Attention selectively reshapes the geometry of distributed semantic representation

Samuel A. Nastase[1,*], Andrew C. Connolly[1,2], Nikolaas N. Oosterhof[3], Yaroslav O. Halchenko[1], J. Swaroop Guntupalli[1], Matteo Visconti di Oleggio Castello[1], Jason Gors[1], M. Ida Gobbini[1,4], James V. Haxby[1,3]

[1]Department of Psychological and Brain Sciences, Dartmouth College, Hanover, NH 03755
[2]Department of Neurology, Geisel School of Medicine at Dartmouth, Hanover, NH 03755
[3]Center for Mind/Brain Sciences, Università degli studi di Trento, 38068 Rovereto, Italy
[4]Department of Medicina Specialistica, Diagnostica e Sperimentale (DIMES), Medical School, University of Bologna, 40126 Bologna, Italy

*Corresponding author:
Samuel A. Nastase
6207 Moore Hall
Hanover, NH
Telephone: (603) 277-0904
Email: samuel.a.nastase.gr@dartmouth.edu

Running title: Attention reshapes representational geometry

Abstract

Humans prioritize different semantic qualities of a complex stimulus depending on their behavioral goals. These semantic features are encoded in distributed neural populations, yet it is unclear how attention might operate across these distributed representations. To address this, we presented participants with naturalistic video clips of animals behaving in their natural environments while the participants attended to either behavior or taxonomy. We used models of representational geometry to investigate how attentional allocation affects the distributed neural representation of animal behavior and taxonomy. Attending to animal behavior transiently increased the discriminability of distributed population codes for observed actions in anterior intraparietal, pericentral, and ventral temporal cortices, while collapsing task-irrelevant taxonomic information. Attending to animal taxonomy while viewing the same stimuli increased the discriminability of distributed animal category representations in ventral temporal cortex and collapsed behavioral information. For both tasks, attention selectively enhanced the categoricity of response patterns along behaviorally relevant dimensions. These findings suggest that behavioral goals alter how the brain extracts semantic features from the visual world. Attention effectively disentangles population responses for downstream read-out by sculpting representational geometry in late-stage perceptual areas.

Keywords: categorization, fMRI, MVPA, natural vision, neural decoding

Introduction

The brain's information processing machinery operates dynamically to accommodate diverse behavioral goals. Selective attention reduces the complexity of information processing by prioritizing representational content relevant to the task at hand (Tsotsos 2011). The attention literature has focused mostly on early vision, employing rudimentary visual stimuli and simple tasks to probe task-related changes in the representation of low-level visual information, such as orientation and motion direction (Carrasco 2011). Humans, however, perceive and act on the world in terms of both semantically-rich representations and complex behavioral goals. Naturalistic stimuli, although less controlled, serve to convey richer perceptual and semantic information, and have been shown to reliably drive neural responses (Hasson et al. 2004; Haxby et al. 2011; Huth et al. 2012, 2016; Guntupalli et al. 2016).

The brain encodes this sort of complex information in high-dimensional representational spaces grounded in the concerted activity of distributed populations of neurons (Averbeck et al. 2006; Kriegeskorte et al. 2008a; Haxby et al. 2014). Population coding is an important motif in neural information processing across species (Dayan and Abbott 2001), and has been well-characterized in early vision (Chen et al. 2006; Miyawaki et al. 2008; Graf et al. 2011), face and object recognition (Rolls and Tovee 1995; Hung et al. 2005; Kiani et al. 2007; Freiwald and Tsao 2010), and other sensorimotor and cognitive domains (Georgopoulos et al. 1986; Lewis and Kristan 1998; Uchida et al. 2000; Rigotti et al. 2013). Multivariate decoding analyses of human neuroimaging data have allowed us to leverage distributed patterns of cortical activation to provide a window into the representation of high-level semantic information (Haxby et al. 2001, 2014; Kriegeskorte et al. 2008a; Mitchell et al. 2008; Oosterhof et al. 2010, 2012; Connolly et al. 2012, 2016; Huth et al. 2012; Sha et al. 2015), but

these studies generally assume that neural representations are relatively stable, rather than dynamic or context-dependent.

Electrophysiological work on attentional modulation has typically been constrained to single neurons (Treue and Martínez Trujillo 1999; Reynolds et al. 2000; Reynolds and Heeger 2009), but more recent work has suggested that task demands may alter population encoding to sharpen attended representations (Cohen and Maunsell 2009; Ruff and Cohen 2014; Downer et al. 2015). In line with this, a handful of recent neuroimaging studies have examined how task demands affect multivariate pattern classification (Serences and Boynton 2007a; Jehee et al. 2011; Brouwer and Heeger 2013; Sprague and Serences 2013; Harel et al. 2014; Erez and Duncan 2015). In particular, Brouwer and Heeger (2013) demonstrated that when participants perform a color naming task, distributed neural representations of color in two early visual areas become more categorical—that is, the neural color space is altered such that within-category distances decrease while between-category colors increase. In a related approach, Çukur and colleagues (2013) used a natural vision paradigm to demonstrate that performing a covert visual search task for either humans or vehicles in natural scenes drives widespread shifts in voxelwise semantic tuning, even when these target objects are not present in the stimulus. With the exception of this study, most prior work has investigated only simple visual stimuli such as oriented gratings, moving dots, colors, and static object images. The current study aims to directly investigate task-related changes in the geometry of distributed neural representation of high-level visual and semantic information about animal taxonomy and behavior conveyed by dynamic, naturalistic stimuli.

We hypothesized that, in order to interface with distributed neural representations, attention may operate in a distributed fashion as well—that is, by selectively reshaping

representational geometry (Edelman 1998; Kriegeskorte and Kievit 2013). This hypothesis was motivated by behavioral and theoretical work suggesting that attention may facilitate categorization by expanding psychological distances along task-relevant stimulus dimensions and collapsing task-irrelevant distinctions (Nosofsky 1986; Kruschke 1992). Here we aimed to provide neural evidence for this phenomenon by examining how task demands affect the distributed neural representation of two types of semantic information thought to rely on distributed population codes: animal taxonomy (Connolly et al. 2012, 2016; Sha et al. 2015) and behavior (Oosterhof et al. 2010, 2012, 2013). We operationalize attention broadly in this context as the modulatory effect of top-down task demands on stimulus-evoked neural representation; at minimum, the 1-back task requires participants to categorize stimuli, maintain the previously observed category in working memory, and compare the currently observed category with the prior category, and execute (or withhold) a motor response. To expand on previous work, we used dynamic, naturalistic video clips of animals behaving in their natural environments. These stimuli not only convey information about animal form or category, but also behavior, allowing us to examine how attention affects the neural representation of observed actions (Oosterhof et al. 2013), which has not previously been studied. Categorical models of representational geometry were employed to demonstrate that attention selectively alters distances between neural representations of both animal taxonomy and behavior along task-relevant dimensions.

Materials and Methods

Participants

Twelve right-handed adults (seven female; mean age = 25.4 ± 2.6 SD years) with normal or corrected-to-normal vision participated in the attention experiment. Participants reported no neurological conditions. Additionally, 19 adults, including the 12 from the attention

experiment, participated in a separate scanning session for the purposes of hyperalignment. All participants gave written, informed consent prior to participating in the study, and the study was approved by the Institutional Review Board of Dartmouth College.

Stimuli and design

Each of the 20 conditions in the fully-crossed design comprised two unique exemplar clips and their horizontally-flipped counterparts, for a total of 40 clips and 80 total exemplars (Supplementary Table 1, Supplementary Video 1). Each trial consisted of a 2 s video clip presented without sound followed by a 2 s fixation period in a rapid event-related design. Clips for the attention experiment were extracted from nature documentaries (*Life*, *Life of Mammals*, *Microcosmos*, *Planet Earth*) and YouTube videos matched for resolution. The clips used in the attention experiment were not included in the segment of the documentary presented for the purpose of hyperalignment. All 80 stimuli, as well as four behavior repetition events, four taxon repetition events, and four null events were presented in pseudorandom order in each of 10 runs, resulting in 92 events per run, plus 12 s fixation before and after the events of interest, for a total run length of 392 s (~6.5 min). Ten unique runs were constructed for a total scan time of approximately 65 min, and run order was counterbalanced across participants. At the beginning of each run, participants were instructed to pay attention to either taxonomy or behavior types and press the button only when they observed a category repetition of that type. There were five behavior attention runs and five taxonomy attention runs presented in counterbalanced order across participants.

For each run, a pseudorandom trial order was first constructed such that no taxonomic or behavioral categories were repeated (adjacent in the trial order). Next, four taxonomic

category repetition events and four behavioral category repetition events were inserted as sparse catch trials such that a repetition event of each type fell on a random trial within each quarter of the run (without inducing unplanned repetitions). Each repetition event repeated either the taxonomic or behavioral category of the preceding stimulus and varied on the other dimension. There were no repetitions of the same clip exemplar (or its horizontal mirror image). Four additional 2 s null events consisting of only a fixation cross were inserted into each run to effect temporal jittering.

The same button was pressed for repetitions of both types. Button presses were only elicited by repetition events and were therefore sparse. Participants were informed that repetition events would be sparse and that they should not pay attention to or press the button if they noticed repetitions of the unattended type. Participants were only instructed to maintain fixation when the fixation cross was present, not during the presentation of the clips.

In an independent scanning session, participants were presented with approximately 63 min of the *Life* nature documentary narrated by David Attenborough for the purpose of hyperalignment. The documentary was presented in four runs of similar duration, and included both the visual and auditory tracks. In the movie session, participants were instructed to remain still and watch the documentary as though they were watching a movie at home. All stimuli were presented using PsychoPy (Peirce 2007).

Image acquisition

All functional and structural images were acquired using a 3 T Philips Intera Achieva MRI scanner (Philips Medical Systems, Bothell, WA) with a 32-channel phased-array SENSE (SENSitivity Encoding) head coil. For the attention experiment, functional images were acquired in an interleaved fashion using single-shot gradient-echo echo-planar imaging with

a SENSE reduction factor of 2 (TR/TE = 2000/35 ms, flip angle = 90°, resolution = 3 mm isotropic, matrix size = 80 × 80, FOV = 240 × 240 mm, 42 transverse slices with full brain coverage and no gap). Each run began with two dummy scans to allow for signal stabilization. For each participant 10 runs were collected, each consisting of 196 dynamic scans totaling 392 s (~6.5 min). At the end of each scanning session, a structural scan was obtained using a high-resolution T1-weighted 3D turbo field echo sequence (TR/TE = 8.2/3.7 ms, flip angle = 8°, resolution = 1 mm isotropic, matrix size = 256 × 256 × 220, FOV = 240 × 188 × 220 mm).

For the movie session, functional images also were acquired in an interleaved order using single-shot gradient-echo echo-planar imaging (TR/TE = 2500/35 ms, flip angle = 90°, resolution = 3 mm isotropic, matrix size = 80 × 80, and FOV = 240 × 240 mm; 42 transverse slices with full brain coverage and no gap). Four runs were collected for each participant, consisting of 374, 346, 377, and 412 dynamic scans, totaling 935 s (~15.6 min), 865 s (~14.4 min), 942.5 s (~15.7 min), and 1030 s (~17.2 min), respectively. At the end of this session, a structural scan was obtained using a high-resolution T1-weighted 3D turbo field echo sequence (TR/TE = 8.2/3.7 ms, flip angle = 8°, resolution = 1 mm isotropic, matrix size = 256 × 256 × 220, and FOV = 240 × 188 × 220). For participants included in both the attention experiment and the movie session, structural images were registered and averaged to increase signal-to-noise ratio.

Preprocessing

For each participant, functional time series data were de-spiked, corrected for slice timing and head motion, normalized to the ICBM 452 template in MNI space, and spatially smoothed with a 4 mm FWHM Gaussian kernel using AFNI (Cox 1996). Functional images

were then motion-corrected in two passes: first, functional images were initially motion corrected, then averaged across time to create a high-contrast reference volume; motion correction parameters were then re-estimated in a second pass using the reference volume as the target. Affine transformation parameters were then estimated to coregister the reference volume and the participant's averaged structural scans. Each participant's averaged structural scan was then normalized to the ICBM 452 template in MNI space. These transformation matrices were concatenated and each participant's data were motion-corrected and normalized to the template via the participant's anatomical scan in a single interpolation step. All subsequent analyses were performed in MNI space. Signal intensities were normalized to percent signal change prior to applying the general linear model.

Functional time series from the *Life* movie session were analyzed using the same preprocessing pipeline. Prior to hyperalignment, time series data were bandpass filtered to remove frequencies higher than 0.1 Hz and lower than 0.0067 Hz. Head motion parameters and the mean time series derived from the FreeSurfer segmentation of the ventricles were regressed out of the signal.

Cortical surfaces were reconstructed from structural scans using FreeSurfer, aligned according to curvature patterns on the spherical surface projection (Fischl et al. 1999), and visualized using SUMA (Saad et al. 2004).

General linear model

A general linear model (GLM) was used to estimate BOLD responses for each of the 20 conditions for each task using AFNI's 3dREMLfit. Stimulus-evoked BOLD responses to each event were modeled using a simple hemodynamic response function (AFNI's GAM response

model) adjusted for a 2 s stimulus duration. Nuisance regressors accounting for repetition events, button presses, and head motion were included in the model. For representational similarity analyses, beta parameters were estimated over the five taxonomy attention runs, then separately over the five behavior attention runs. Time points subtending abrupt head movements greater than roughly 1 mm of displacement or 1 degree of rotation were censored when fitting the general linear model. For each of the two attention conditions, the stimulus-evoked response pattern for each taxonomic–behavioral category condition was estimated from 20 trials presented in pseudorandom order over the course of five separate runs (interspersed with runs from the other attention condition). Therefore we expect these response patterns (and the subsequent neural RDMs) to be relatively robust to instrumental noise, temporal autocorrelation and intrinsic physiological correlations in the preprocessed time series data (Henriksson et al. 2015). Betas for each voxel were z-scored across the 20 conditions per feature before and after hyperalignment, and prior to any multivariate analysis. Note that constructing neural RDMs by computing the correlation distance between response pattern vectors (rather than, e.g., Euclidean distance) entails that the subsequent multivariate analyses are invariant to differences in regional-average activity levels within a searchlight or ROI (Kriegeskorte et al. 2008b). For searchlight classification analyses (Supplementary Fig. 2), beta parameters were estimated separately for each run.

Whole-brain hyperalignment

Surface-based searchlight whole-brain hyperalignment (Haxby et al. 2011; Guntupalli et al. 2016) was performed based on data collected while participants viewed the *Life* nature documentary. Each surface-based searchlight referenced the 200 nearest voxels from the associated volume, selected based on their geodesic proximity to the searchlight center. The time series of response patterns elicited by the movie stimulus was rotated via the

Procrustes transformation in order to achieve optimal functional alignment across participants and the estimated transformation matrices for each searchlight were aggregated (Supplementary Fig. 1*A*). Hyperalignment transformation parameters estimated from the movie data were then applied to the independent attention experiment data. Subsequent analyses were applied to the hyperaligned data. All multivariate pattern analyses were performed using the PyMVPA package (www.pymvpa.org; Hanke et al. 2009).

Searchlight representational similarity regression

Representational similarity analysis (Kriegeskorte et al. 2008b) was applied using 100-voxel surface-based searchlights (Kriegeskorte et al. 2006; Oosterhof et al. 2011). Each surface-based searchlight referenced the 100 nearest voxels to the searchlight center based on geodesic distance on the cortical surface. Pairwise correlation distances between stimulus-evoked response patterns for the 20 conditions were computed separately for each task. These pairwise distances were collated into a representational dissimilarity matrix (RDM) describing the representational geometry for a patch of cortex (Kriegeskorte and Kievit 2013).

Two categorical target RDMs were constructed based on the experimental design: one of these RDMs discriminated the animal taxa invariant to behavior, the other discriminated the behaviors invariant to taxonomy. Least squares multiple regression was then used to model the observed neural RDM as a weighted sum of the two categorical target RDMs. For each searchlight, both the observed neural RDM and the target RDMs were ranked and standardized prior to regression (see Saltelli et al. 2004). Since we suspect the neural representational space does not respect the magnitude of dissimilarity specified by our models, we relax the linear constraint and ensure only monotonicity (analogous to Spearman

correlation, keeping with Kriegeskorte et al. 2008b). Although applying the rank transform prior to least squares linear regression is relatively common practice, this approach may emphasize main effects at the expense of interaction effects; however, in the current experiment, we have no a priori hypotheses corresponding to interaction terms. Intercept terms in the estimated models were negligible across all searchlights, task conditions, and participants. The searchlight analysis was performed in the hyperaligned space, then the results were projected onto the cortical surface reconstruction for the participant serving as the reference participant in the hyperalignment algorithm.

Statistical assessment of searchlight analysis

To assess the statistical significance of searchlight maps across participants, all maps were corrected for multiple comparisons without choosing an arbitrary uncorrected threshold using threshold-free cluster enhancement (TFCE) with the recommended values (Smith and Nichols 2009). A Monte Carlo simulation permuting condition labels was used to estimate a null TFCE distribution (Oosterhof et al. 2012). First, 100 null searchlight maps were generated for each participant by randomly permuting condition labels within each observed searchlight RDM; then 10,000 null TFCE maps were constructed by randomly sampling from these null data sets in order to estimate a null TFCE distribution.

The resulting searchlight maps are thresholded at $p = .05$ corrected for familywise error using TFCE, and the average regression coefficient across participants is plotted for surviving searchlights. In the case of searchlight classification (Supplementary Fig. 2), labels were shuffled within each run and each category of the crossed factor (e.g., the four behavior labels were permuted within each of the five taxa), then the full cross-validation scheme was applied (Nastase et al. 2016). The resulting maps are similarly thresholded, with the average

classification accuracy across participants plotted for surviving searchlights. For difference maps (Supplementary Fig. 3), clusters surviving correction for multiple comparisons are indicated by white contours and subthreshold searchlights are displayed transparently. This method for multiple comparisons correction was implemented using the CoSMoMVPA software package (cosmomvpa.org; Oosterhof et al. 2016).

To assess more global effects, task-related differences in regression coefficients across searchlights were computed separately for each categorical target RDM. For the behavioral category target RDM, the mean regression coefficients were computed across all searchlight regression coefficients surviving TFCE in both attention conditions, and a nonparametric randomization test was used to evaluate the significance of a task difference in the mean regression coefficient across participants. This procedure was repeated for the taxonomic category target RDM considering all searchlight regression coefficients that survived TFCE in both tasks.

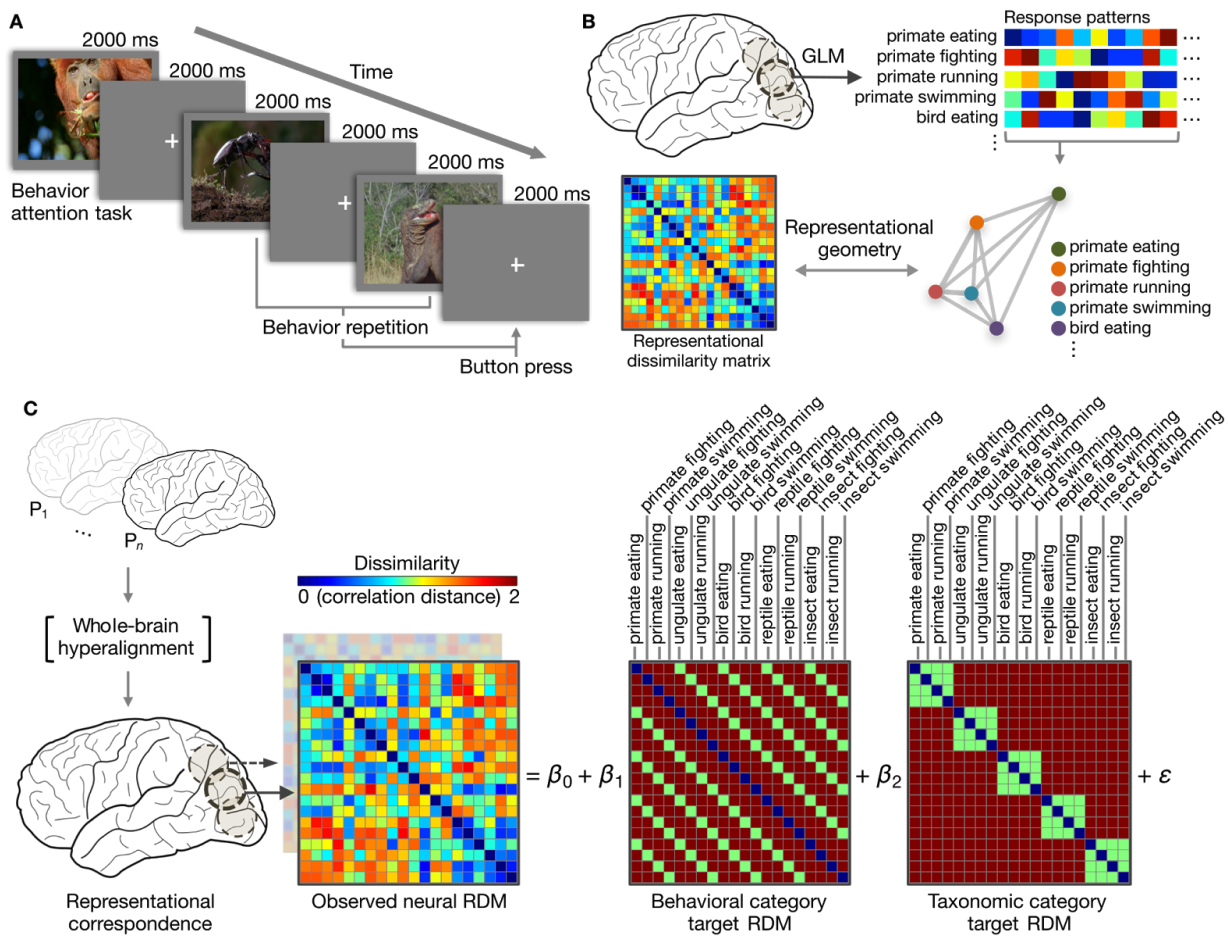

Figure 1. Experimental procedure and analytic approach. (*A*) Schematic of event-related design with naturalistic video clips of behaving animals (Supplementary Table 1, Supplementary Video 1). Participants performed a repetition detection task requiring them to attend to either animal taxonomy or behavior. (*B*) Stimulus-evoked response patterns for the 20 conditions were estimated using a conventional general linear model. The pairwise correlation distances between these response patterns describe the representational geometry (representational dissimilarity matrix; RDM) for a given brain area. (*C*) Whole-brain surface-based searchlight hyperalignment was used to rotate participants' responses into functional alignment based on an independent scanning session (Supplementary Fig. 1).

Following hyperalignment, the neural representational geometry in each searchlight was modeled as a weighted sum of models capturing the taxonomic and behavioral categories.

Identifying regions of interest

Cluster analysis was used to identify regions of the cortical surface characterized by shared representational geometry in an unsupervised manner (Connolly et al. 2012). Prior to cluster analysis, the observed neural RDMs for each surface-based searchlight were converted from correlation distances to Fisher transformed correlation values and averaged across participants. Gaussian mixture models were used to cluster searchlights according to their representational geometry at varying values of *k* components (clusters). Gaussian mixture modeling is a probabilistic generalization of the *k*-means algorithm, and models the 20,484 searchlights as a mixture of *k* overlapping Gaussian distributions in a 190-dimensional feature space defined by the upper triangular of the 20 × 20 observed neural RDM. The clustering algorithm was implemented using the scikit-learn machine learning library for Python (Pedregosa et al. 2011).

We evaluated the reproducibility of parcellations across participants at values of *k* from 2 to 30 using a split-half resampling approach (100 iterations per *k*) that has previously been applied to functional parcellations based on resting-state functional connectivity (Yeo et al. 2011). For each of 100 resampling iterations, half of the participants were randomly assigned to a training set, while the other half were assigned to a test set (Lange et al. 2004). Surface-based searchlight RDMs for each participant were then averaged across participants within the separate training and test sets. Gaussian mixture models were estimated on the training set for each of *k* components ranging from 2 to 30. Test data were

then assigned to the nearest cluster mean of the model estimated from the training data. A separate mixture model was then estimated for the test data, and the predicted cluster labels (based on the training data) were compared to the actual cluster labels using adjusted mutual information (AMI; Thirion et al. 2014). AMI compares cluster solutions and assigns a value between 0 and 1, where 0 indicates random labeling and 1 indicates identical cluster solutions (robust to a permutation of labels, adjusted for greater fit by chance at higher *k*). Note that, unlike previous applications (Yeo et al. 2011), we cross-validated AMI at the participant level rather than partitioning at the searchlight level.

Separate parcellations were obtained for each attention task condition to ensure the clustering algorithm did not attenuate task effects. The cluster analysis yielded qualitatively similar surface parcellations for data from both the behavior attention task and the taxonomy attention task, however the behavior attention task tended toward more reproducible solutions at higher *k*. Note that clustering cortical searchlights according to the pairwise neural distances between a certain set of experimental conditions should not be expected to yield a generally valid parcellation for the entire brain. Furthermore, although spatial smoothing, overlapping searchlights, and hyperalignment induce spatial correlations, there is nothing intrinsic to the clustering algorithm that ensures spatial contiguity (on the cortical surface) or bilaterality in the resulting parcellation.

The reproducibility analysis indicated local maxima at k = 2, 4, 14, 19, and 23 (Supplementary Fig. 4*A*), and these cluster solutions can then be mapped back to the cortical surface (Supplementary Figs. 4*B*, 5). All subsequent analyses were performed on regions of interest (ROIs) derived from the parcellation at k = 19 based on the behavior attention data. From these 19 areas tiling the entire cortical surface, 10 ROIs were selected

comprising early visual areas, the ventral visual pathway, the dorsal visual pathway, and somatomotor cortex. These 10 ROIs corresponded to the areas of the brain with the highest inter-participant correlation of RDMs for both tasks (Supplementary Fig. 1*D*). Both the clustering algorithm and the reproducibility analysis are agnostic to any particular representational geometry or task effect (Kriegeskorte et al. 2009). ROIs were large, including on average 1,980 voxels (SD = 1,018 voxels; see Supplementary Table 2 for individual ROI extents).

Correlations with target RDMs

For each ROI, we used the stimulus-evoked patterns of activation across all referenced voxels to compute neural RDMs for both attention conditions. We tested for task differences in Spearman correlation between the observed neural RDM and the target RDMs. To test this, we first constructed a linear mixed-effects model to predict Spearman correlations with the categorical target RDMs using Task, Target RDM, and ROI, and their two- and three-way interactions as fixed effects, with Participant modeled as a random effect (random intercepts). The Task variable captured the two attentional task conditions, Target RDM represented the behavioral and taxonomic category target RDMs, and ROI represented the 10 regions of interest. Mixed-effects modeling was performed in R using *lme4* (Bates et al. 2015). Statistical significance was assessed using a Type III analysis of deviance. To assess the statistical significance of differences in Spearman correlation as a function of attention task for each ROI, nonparametric randomization tests were performed in which the mean difference in correlation was computed for all possible permutations of the within-participants attention task assignments (2^{12} = 4,096 permutations, exact test).

Evaluating model fit

As evidenced by the searchlight analysis (Fig. 2), the target RDMs for taxonomy and observed behavior representation may differ in the extent to which they capture neural representational geometry. To address this, we evaluated differences in the fit of these models. However, although the target RDMs were sufficient to test our hypothesis, they cannot capture differences in the distances between behavioral and taxonomic categories; e.g., the animacy continuum (Connolly et al. 2012; Sha et al. 2015). To accommodate this type of geometry for behavior and taxonomy, we decomposed the categorical target RDMs into separate regressors for each between-category relationship (six regressors for behavior model, 10 for the taxonomy model). For example, the taxonomy model consists of a separate regressor for each within-category "box" along the diagonal of the taxonomic category target RDM (Fig. 1).

To evaluate these two flexible behavior and taxonomy models, in each ROI and each participant we computed the coefficient of partial determination (partial R^2), then averaged these model fits over the two attention tasks (van den Berg et al. 2014). Partial R^2 can be interpreted as the proportion of variance accounted for by one model controlling for any variance accounted for by the other model, and was computed separately for each attention task and then averaged across tasks within participants. We then computed the within-participants differences between the two models per ROI, and submitted these differences to a nonparametric randomization test to assess significance across participants. Note, however, that partial R^2 is biased toward more complex models (in this case, the taxonomy model), so we corroborated this analysis using the Akaike information criterion (AIC), which penalizes more complex models. We computed the difference in AIC for the six- and 10-regressor models for each attention task condition within each participant, then

averaged across the attention tasks. These differences in AIC were assessed statistically using an exact test permuting the sign of the difference.

Task-related differences in representational distances

Next, we probed for task-related differences in representational distances directly. Note however that certain pairwise distances (e.g., the distance between neural representations of a bird eating and an insect fighting) would not be hypothesized to change in a meaningful way as a function of our task manipulation (see, e.g., the diagonal distances in Fig. 4*B*). For this reason, we constrained our analysis to only within-category pairwise distances (cells of the RDM). Correlation distances were converted to Fisher-transformed correlations prior to statistical testing. Rather than averaging the pairwise distances across cells of the target RDM within each participant, cells corresponding to particular pairwise distances were included as a random effect (as per an items analysis; Baayen et al. 2008). We constructed a linear mixed-effects model to predict observed correlation distances based on Task, Category, and ROI, and their two- and three-way interactions as fixed effects, with Participant and Cell as random effects (random intercepts). Task represented the attentional task condition, Category represented the category relationship (within-behavior or within-taxon), ROI indicated the 10 ROIs reported above, and Cell indicated particular cells (pairwise relationships) of the target RDM. Statistical significance was assessed using a Type III analysis of deviance. Nonparametric randomization tests were used to assess task-related differences in mean within-category correlation distances within each ROI.

Visualizing neural representational space

To visualize task-related changes in representational geometry, we used multidimensional scaling (Kriegeskorte et al. 2008b). For a given ROI, we first computed 40 × 40 neural RDMs

based on the 20 conditions for both attention tasks and averaged these across participants. To visualize task-related changes in observed action representation, we computed an 8 × 8 distance matrix comprising the mean between-behavior distances within each taxonomic category (as in Fig. 4). For taxonomy representation, we computed the average between-taxon distances within each behavioral category to construct a 10 × 10 matrix. Distances were computed between conditions for both tasks (e.g., resulting in a single 8 × 8 distance matrix rather than two separate 4 × 4 matrices for behavior representation) to ensure that distances for both attention tasks were on the same scale.

These distance matrices were then submitted to metric multidimensional scaling implemented in scikit-learn (Pedregosa et al. 2011). In the case of behavior representation, for example, this resulted in eight positions in a two-dimensional space. However, because we were interested in the overall task-related expansion between conditions (and less concerned with, e.g., the distance between one condition in one attention task and another condition in the other attention task), the positions in the resulting two-dimensional solution were then split according to attention task, and the Procrustes transformation (without scaling) was used to best align the conditions within one attention task to another. This transformation preserves the relationships between conditions within each task and captures the overall attentional expansion of between-category distances.

Results

Behavioral performance

Participants were highly accurate in detecting the sparse repetition events for both attention conditions (mean accuracy for animal attention condition = 0.993, SD = 0.005; mean accuracy for behavior attention condition = 0.994, SD = 0.005). There was no significant

task-related difference in either accuracy ($t(11) = 0.469$, $p = 0.648$), or signal detection theoretic measures of sensitivity ($t(11) = 0.116$, $p = 0.910$) and bias ($t(11) = 0.449$, $p = 0.662$) adjusted for logistic distributions.

Searchlight analysis

We applied representational similarity analysis using surface-based searchlights to map areas of the brain encoding information about animal taxonomy and behavior. Neural representational dissimilarity matrices (RDMs) were computed based on the pairwise correlation distances between hyperaligned stimulus-evoked response patterns for the 20 conditions (Fig. 1*B*). We modeled the neural representational geometry as a weighted sum of two categorical target RDMs reflecting the experimental design: a behavioral category target RDM and a taxonomic category target RDM (Fig. 1*C*).

Regression coefficients for the behavioral category target RDM were strongest in lateral occipitotemporal (LO) cortex, in the dorsal visual pathway subsuming posterior parietal, intraparietal sulcus (IPS), motor and premotor areas, and in ventral temporal (VT) cortex (Fig. 2*A*). Regression coefficients for the animal taxonomy target RDM were strongest in VT, LO, and posterior parietal cortices, as well as left inferior and dorsolateral frontal cortices. Globally, attending to behavior or taxonomy increased the regression coefficients for the target RDMs corresponding to the attended categories. Attending to behavior increased the number of searchlights with significant regression coefficients for the behavioral category target RDM from 11,408 to 14,803 (corrected for multiple comparisons). When considering regression coefficients for the behavioral category target RDM in all searchlights surviving multiple comparisons correction for either attention task, attending to animal behavior significantly increased the mean regression coefficient from 0.100 to 0.129 ($p = .007$,

nonparametric randomization test). Attending to taxonomy increased the number of searchlights with significant regression coefficients for the taxonomic category target RDM from 1,691 to 3,401. For searchlights surviving multiple comparisons correction for either task, regression coefficients for the taxonomic category RDM increased significantly from 0.049 to 0.071 (p = .017, nonparametric randomization test). A linear SVM searchlight classification analysis, in which we used leave-one-category-out data folding for cross-validation (Supplementary Fig. 2), resulted in qualitatively similar maps, suggesting the results presented in Fig. 2 are not driven solely by low-level visual properties of particular stimuli (although low-level visual properties may still covary with condition).

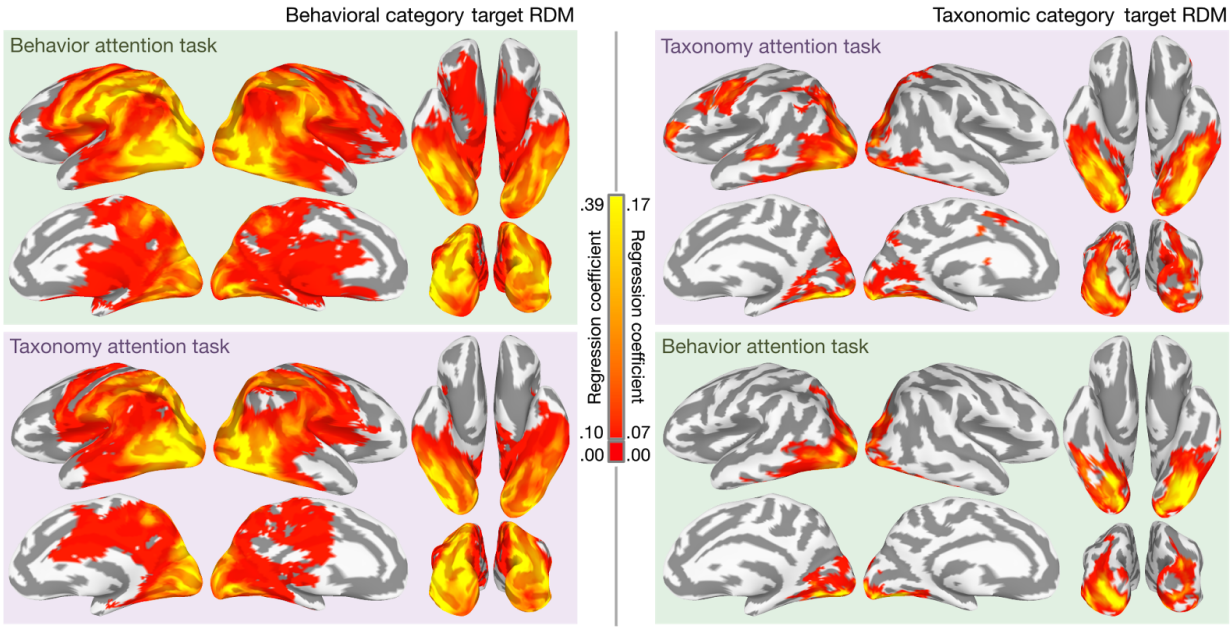

Figure 2. Mapping representations of animal behavior and taxonomy for both tasks. Significant searchlight regression coefficients for the behavioral category target RDM (left) and the taxonomic category target RDM (right) are mapped onto the cortical surface for both attention conditions. Cluster-level significance was assessed at the group level using TFCE and maps are thresholded at $p < .05$ (nonparametric one-sided test, corrected for multiple

comparisons). For searchlights surviving cluster-level significance testing, the mean regression coefficient across participants is plotted. Note that regression coefficients for behavior representation and taxonomy representation are plotted with different color scales to better visualize the distribution of coefficients. Regression coefficients less than 0.10 for the behavioral category target RDM and less than 0.07 for the taxonomic category target RDM are plotted as red. See Supplementary Fig. 2 for qualitatively similar searchlight classification maps, and Supplementary Fig. 3 for difference maps.

Regions of interest

We tested our hypothesis in larger ROIs defined by shared searchlight representational geometry. We applied an unsupervised clustering algorithm to the searchlight representational geometries to parcellate cortex into ROIs and used a relatively reproducible parcellation with 19 areas (Supplementary Fig. 4). We interrogated 10 ROIs with high inter-participant similarity of searchlight representational geometry subtending the dorsal and ventral visual pathways (Fig. 3*B*, Supplementary Fig. 1) . The 10 ROIs were labeled as follows: posterior early visual cortex (pEV), inferior early visual cortex (iEV), superior early visual cortex (sEV), anterior early visual cortex (aEV), lateral occipitotemporal cortex (LO), ventral temporal cortex (VT), occipitoparietal and posterior parietal cortex (OP), intraparietal sulcus (IPS), left postcentral sulcus (left PCS), and ventral pericentral and premotor cortex (vPC/PM).

For each ROI, we measured the Spearman correlation between the observed neural RDM and the two categorical target RDMs for each task (Fig. 3*A*). A linear mixed-effects model yielded significant main effects for ROI ($\chi^2(9) = 115.690$, $p < .001$) and Target RDM ($\chi^2(9) =$

69.640, $p < .001$), while the Target RDM × ROI interaction was significant ($\chi^2(9) = 112.442$, $p < .001$). The Task × ROI interaction was also significant ($\chi^2(9) = 23.301$, $p = .006$), suggesting that the task manipulation more strongly affected correlations in certain ROIs than others. Finally, the three-way Task × Target RDM × ROI interaction was significant ($\chi^2(9) = 22.034$, $p = .009$), motivating the following within-ROI tests. Nonparametric randomization tests revealed that attending to animal behavior increased correlations between the observed neural RDM and the behavioral category target RDM in vPC/PM ($p = .026$), left PCS ($p = .005$), IPS ($p = .011$), and VT ($p = .020$). A decrease in the categoricity of behavior representation was observed in sEV when participants attended to behavior ($p = .032$). Attending to animal taxonomy increased correlations between the observed neural RDM and the taxonomic category target RDM in VT ($p = 0.010$) and left PCS ($p = .036$). The effect in left PCS was driven by a negative correlation in the behavior attention task that was abolished when attention was directed at taxonomy. Supplementary Tables 2 and 3 present task differences in Spearman correlation for all 19 parcels returned by the cluster analysis and all anatomically discontiguous parcels, respectively.

We next evaluated how well full representational models of animal taxonomy and behavior fit the neural representational geometry in each ROI. The model RDMs used above tested our experimental hypothesis but do not capture the geometry of distances between behavioral or taxonomic categories; e.g., the animacy continuum (Connolly et al. 2012; Sha et al. 2015). To accommodate this type of geometry for behavior and taxonomy, we decomposed the categorical target RDMs into separate regressors for each pairwise between-category similarity (six regressors for behavior model, 10 for the taxonomy model). To evaluate these two flexible behavior and taxonomy models, in each ROI we estimated the coefficient of partial determination (partial R^2) and AIC separately for each model and attention task within

each participant, then averaged these model fits over the two attention tasks. The six-regressor behavior model captured on average over 2 times more variance (adjusted R^2) than the single-regressor behavioral category target RDM in LO, VT, OP, IPS, left PCS, and vPC/PM, suggesting that some behaviors are more similar to each other than are others. The 10-regressor taxonomy model accounted for well over 4 times more variance than the single-regressor taxonomic category target RDM in pEV, iEV, and VT. Based on nonparametric randomization tests, partial R^2 for the behavior model significantly exceeded that of the animal taxonomy model in sEV, LO, VT, OP, IPS, left PCS, and vPC/PM (Fig. 3*C*), and AIC for the behavior model was significantly lower for all 10 ROIs. Surprisingly, the behavior model accounted for over 2.5 times more variance in VT neural representational geometry than did the taxonomy model (behavior model: 23.8% of variance; taxonomy model: 8.8% of variance).

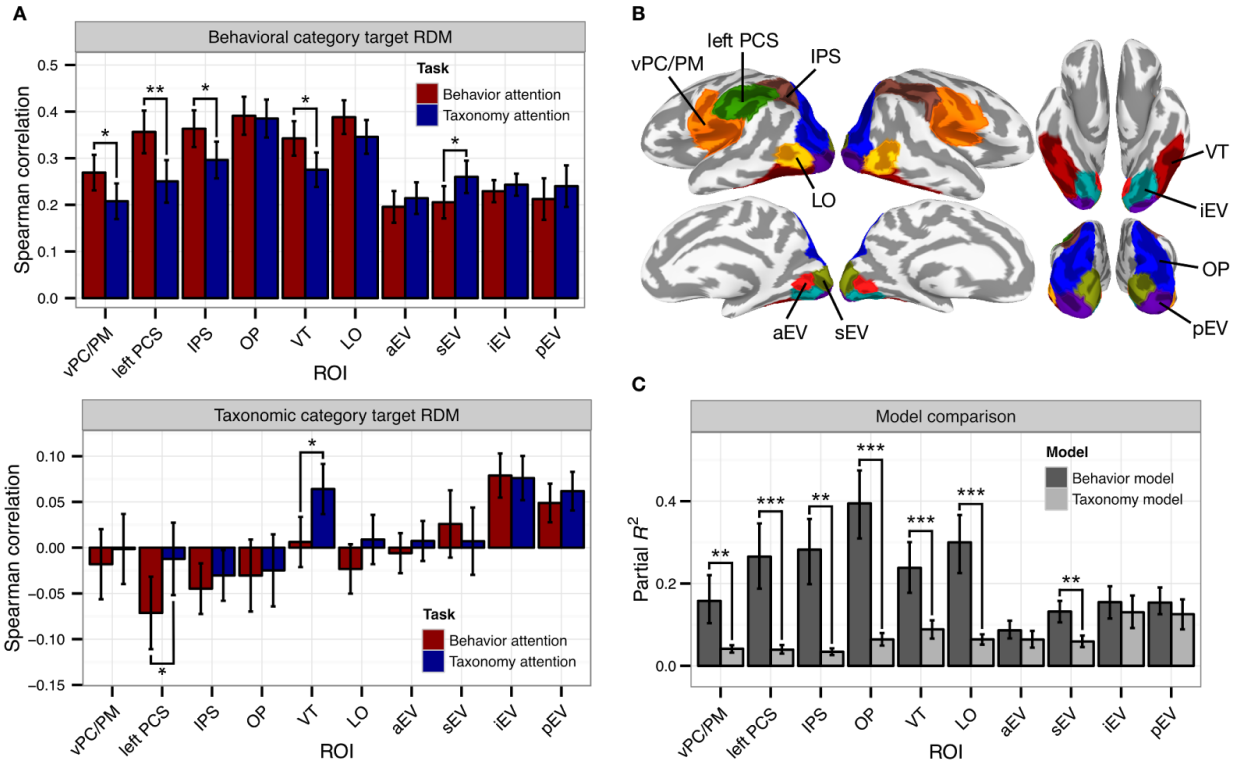

Figure 3. Attention alters representational geometry in functionally-defined ROIs. (*A*) Task differences in Spearman correlation between neural RDMs and the behavioral and taxonomic category target RDMs (see Supplementary Table 2 for results for all 19 clusters). All error bars indicate bootstrapped 95% confidence intervals for within-participants comparisons. (*B*) Ten functional ROIs identified by parcellating the cerebral cortex based on representational geometry. (*C*) Comparison of model fit for the six-regressor behavior model and 10-regressor taxonomy model. $^{*}p < .05$, $^{**}p < .01$, $^{***}p < .001$, two-sided nonparametric randomization test.

We next isolated cells of the neural RDM capturing distances between two conditions that differed on one dimension and were matched on the other; i.e., different behaviors performed by animals from the same taxonomic category, or animals of different taxonomic categories performing the same behavior (Fig. 4*A*). Although we hypothesized that attention expands the distances between task-relevant representations and collapses the distances between task-irrelevant representations as depicted in Fig. 4*B* (40, 41), note that diagonal distances do not change; that is, the effect of attention on distances between conditions that differ on both dimensions is ambiguous. Thus, focusing on the correlation distances between pairs of conditions that differ on only one dimension affords a more unconfounded examination of the effects of attention. A significant increase in, e.g., between-taxon correlation distances within each behavior (Fig. 4*A*, red) when attending to behavior can also be interpreted as a decrease in within-taxon distances when attending to taxonomy; therefore, we refer to this effect as enhancing categoricity. A linear mixed-effects model yielded significant main effects for ROI ($\chi^2(9) = 66.850$, $p < .001$) and Category

(within-behavior or within-taxon category relationship; $\chi^2(9) = 13.047$, $p < .001$), as well as a significant ROI × Category interaction ($\chi^2(9) = 165.725$, $p < .001$). Most importantly, this analysis revealed a significant three-way Task × Category × ROI interaction ($\chi^2(9) = 33.322$, $p < .001$), motivating the following within-ROI tests. Nonparametric randomization tests indicated that attention significantly enhanced categoricity for both groups of distances in left PCS (between-taxon, within-behavior distances: $p = .002$; between-behavior, within-taxon distances: $p = .010$) and VT (between-taxon, within-behavior distances: $p = .028$; between-behavior, within-taxon distances: $p = .009$). Attention significantly enhanced the categoricity of between-taxon distances within behaviors in vPC/PM ($p = .007$), effectively collapsing taxonomic distinctions when attending to behavior. An inverted task effect was observed in sEV (between-taxon, within-behavior distances: $p = .028$). Supplementary Tables 4 and 5 present the task enhancement of representational distances for all 19 parcels returned by cluster analysis and all anatomically discontiguous parcels, respectively. The expansion of distances between attended category representations is illustrated with multidimensional scaling of the representational geometries in left PCS and VT (Fig. 4*C*).

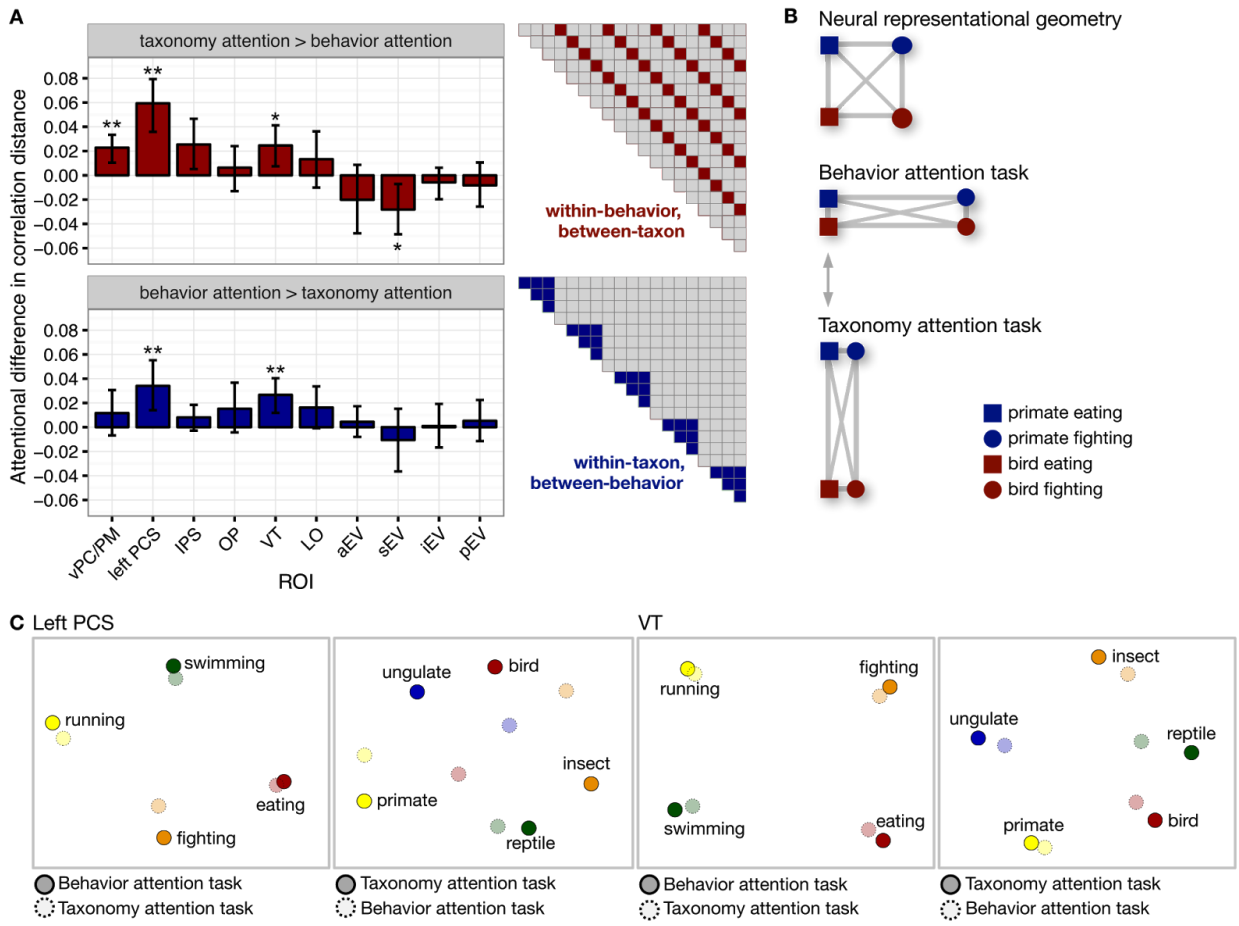

Figure 4. Attention enhances the categoricity of neural responses patterns. (*A*) Enhancement of within-category distances for both behavioral and taxonomic categories based on the attention task (see Supplementary Table 3 for results for all 19 clusters). Error bars indicate bootstrapped 95% confidence intervals. (*B*) Schematic illustrating how neural distances are expanded along the behaviorally relevant dimensions while task-irrelevant distances are collapsed (Nosofsky 1986; Kruschke 1992). (*C*) Multidimensional scaling (MDS) solutions for left PCS and VT depict the attentional expansion of between-category distances. *$p < .05$, **$p < .01$, two-sided nonparametric randomization test.

Discussion

The present study was motivated by the following question: How does attention prioritize certain semantic features of a complex stimulus in service of behavioral goals? We hypothesized that attention may enhance certain features of semantic information encoded in distributed neural populations by transiently altering representational geometry (Kriegeskorte and Kievit 2013). Our findings provide neural evidence for psychological theories of attentional deployment in categorization (Nosofsky 1986; Kruschke 1992) by demonstrating that attention selectively increases distances between stimulus-evoked neural representations along behaviorally relevant dimensions. To expand on prior work examining early visual (e.g., orientation, contrast, color, motion direction; Serences and Boynton 2007b; Jehee et al. 2011; Brouwer and Heeger 2013; Sprague and Serences 2013) and object category (Çukur et al. 2013; Harel et al. 2014; Erez and Duncan 2015) representation, we used dynamic, naturalistic stimuli to demonstrate that attention alters the representation of both animal taxonomy and behavior according to a similar principle.

When participants attended explicitly to animal behavior, the categoricity of observed action representation increased most dramatically in premotor, pericentral, and postcentral somatomotor areas supporting action recognition (Oosterhof et al. 2010, 2012, 2013), intraparietal areas implicated in executive control (Petersen and Posner 2012), and VT. In the current study, we cannot rule out the possibility that attending to behavior enhances the representation of low-level motion-related features of the stimulus more so than higher-level semantic representations. However, we note that retinotopic visual areas driven primarily by motion energy (Nishimoto et al. 2011; Huth et al. 2012) and early areas exhibiting robust representation of animal behavior (e.g., LO and OP) were not strongly modulated by the task manipulation. Attending to animal taxonomy increased the categoricity of animal

representation in VT, consistent with accounts of neural representation of animals and objects (Connolly et al. 2012; Grill-Spector and Weiner 2014; Sha et al. 2015), as well as left PCS, but not in lateral occipitotemporal or early visual areas. Note that attending to behavior induced a negative correlation for the taxonomic category target RDM in left PCS, while attending to taxonomy abolished this effect. This negative correlation when attending to behavior could be driven by increased distances between behavior representations within each animal taxon.

Performing a categorization task requiring attention to either animal taxonomy or behavior enhances the categoricity of neural representations by accentuating task-relevant distinctions and reducing unattended distinctions. Our results demonstrate that attentional allocation sculpts representational geometry in late-stage sensorimotor areas, and this effect was not observed in early perceptual areas. Our results demonstrate that the representational geometry of semantic information in systems such as VT and somatomotor cortex is dynamic and actively tuned to behavioral goals, rather than being solely a reflection of static conceptual knowledge.

Numerous visual areas coded for both taxonomy and behavior, suggesting these two types of information are encoded in distributed population codes in a superimposed or multiplexed fashion (Grill-Spector and Weiner 2014; Haxby et al. 2014). However, the behavior model accounted for notably more variance in neural representation throughout the cortex than the taxonomy model—even in areas typically associated with animal category representation, such as VT (Connolly et al. 2012; Sha et al. 2015). This may in part be due to the heterogeneity of exemplar species within each taxon and the prevalence of motion energy information when viewing naturalistic video stimuli (Huth et al. 2012). Work by others shows,

however, that lateral fusiform cortex responds strongly to dynamic stimuli that depict agentic behavior with no biological form (Grossman and Blake 2002; Gobbini et al. 2007), and biological motion and social behaviors drive responses in face-selective temporal areas in the macaque (Russ and Leopold 2015).

The present study expands on work by (Brouwer and Heeger 2013) demonstrating that the neural color space in early visual areas becomes more categorical when participants perform a color naming task. Here, we use rich, naturalistic stimuli to demonstrate that task demands affect neural representations of animal taxonomy and behavior in a similar fashion in perceptual and somatomotor areas. The current findings also complement a recent study by Çukur and colleagues (2013) demonstrating that attending to a particular object category (humans or vehicles) shifts the semantic tuning of widely distributed cortical voxels toward that category, even when exemplars of that category are not present in the stimulus. Although the tuning shifts observed by Çukur and colleagues (2013) are consistent with a selective expansion of representational space, they may not be the exclusive underlying mechanism. For example, increased response gain, sharper tuning (Brouwer and Heeger 2013), and changes in the correlation structure among voxels (Chen et al. 2006; Miyawaki et al. 2008) may also contribute to the task-related differences we observe in distributed representation. Further work is needed to investigate the relative roles played by each of these candidate mechanisms in task-related changes of representational geometry measured from distributed response patterns. Nonetheless, our findings provide a direct demonstration of the task-related expansion of representational space hypothesized by Çukur and colleagues (2013) and extend the domain of attentional modulation from object categories to observed actions.

Scaling up the effects of attention on single neurons to population responses and multivoxel patterns of activity is an outstanding challenge. Top-down signals (Desimone and Duncan 1995; Baldauf and Desimone 2014) may bias how information is encoded at the population level by altering neuronal gain, tuning, and interneuronal correlations (Averbeck et al. 2006; Cohen and Maunsell 2009; Ruff and Cohen 2014; Downer et al. 2015) in order to optimize representational discriminability for downstream read-out systems. Our findings suggest a model whereby attention alters population encoding in late-stage perception so as to enhance the discriminability of task-relevant representational content. At an algorithmic level (Marr 1982), attention may tune a feature space of arbitrary dimensionality by dynamically altering population encoding. This mechanism could enhance behavioral performance by temporarily disentangling (DiCarlo et al. 2012) task-relevant representations and collapsing task-irrelevant content.

Funding

This work was supported by the National Institute of Mental Health at the National Institutes of Health (grant numbers F32MH085433-01A1 to A.C.C.; and 5R01MH075706 to J.V.H.), and by the National Science Foundation (grant number NSF1129764 to J.V.H.).

Acknowledgments

We thank Kelsey Wheeler for help in collecting the video stimuli and Courtney Rogers for administrative support.

Author Contributions

S.A.N. and J.V.H. designed research; S.A.N. performed research; A.C.C., N.N.O., Y.O.H., J.S.G., M.V.D.O.C., J.G., and M.I.G. contributed analytic tools; S.A.N. analyzed data; and S.A.N. and J.V.H. wrote the paper.

References

Averbeck BB, Latham PE, Pouget A. 2006. Neural correlations, population coding and computation. Nat Rev Neurosci. 7:358–366.

Baayen RH, Davidson DJ, Bates DM. 2008. Mixed-effects modeling with crossed random effects for subjects and items. J Mem Lang. 59:390–412.

Baldauf D, Desimone R. 2014. Neural mechanisms of object-based attention. Science. 344:424–427.

Bates D, Maechler M, Bolker B, Walker S. 2015. lme4: Linear mixed-effects models using Eigen and S4 (Version 1.1-7) [WWW Document]. URL http://CRAN.R-project.org/package=lme4

Brouwer GJ, Heeger DJ. 2013. Categorical clustering of the neural representation of color. J Neurosci. 33:15454–15465.

Carrasco M. 2011. Visual attention: The past 25 years. Vision Res. 51:1484–1525.

Chen Y, Yuzhi C, Geisler WS, Eyal S. 2006. Optimal decoding of correlated neural population responses in the primate visual cortex. Nat Neurosci. 9:1412–1420.

Cohen MR, Maunsell JHR. 2009. Attention improves performance primarily by reducing interneuronal correlations. Nat Neurosci. 12:1594–1600.

Connolly AC, Guntupalli JS, Gors J, Hanke M, Halchenko YO, Wu Y-C, Abdi H, Haxby JV. 2012. The representation of biological classes in the human brain. J Neurosci.

32:2608–2618.

Connolly AC, Sha L, Guntupalli JS, Oosterhof N, Halchenko YO, Nastase SA, di Oleggio Castello MV, Abdi H, Jobst BC, Gobbini MI, Haxby JV. 2016. How the human brain represents perceived dangerousness or “predacity” of animals. J Neurosci. 36:5373–5384.

Cox RW. 1996. AFNI: software for analysis and visualization of functional magnetic resonance neuroimages. Comput Biomed Res. 29:162–173.

Çukur T, Nishimoto S, Huth AG, Gallant JL. 2013. Attention during natural vision warps semantic representation across the human brain. Nat Neurosci. 16:763–770.

Dayan P, Abbott LF. 2001. Theoretical Neuroscience: Computational and Mathematical Modeling of Neural Systems. Cambridge, MA: MIT Press.

Desimone R, Duncan J. 1995. Neural mechanisms of selective visual attention. Annu Rev Neurosci. 18:193–222.

DiCarlo JJ, Zoccolan D, Rust NC. 2012. How does the brain solve visual object recognition? Neuron. 73:415–434.

Downer JD, Niwa M, Sutter ML. 2015. Task engagement selectively modulates neural correlations in primary auditory cortex. J Neurosci. 35:7565–7574.

Edelman S. 1998. Representation is representation of similarities. Behav Brain Sci. 21:449–467.

Erez Y, Duncan J. 2015. Discrimination of Visual Categories Based on Behavioral Relevance in Widespread Regions of Frontoparietal Cortex. J Neurosci. 35:12383–12393.

Fischl B, Sereno MI, Tootell RB, Dale AM. 1999. High-resolution intersubject averaging and a coordinate system for the cortical surface. Hum Brain Mapp. 8:272–284.

Freiwald WA, Tsao DY. 2010. Functional compartmentalization and viewpoint generalization

within the macaque face-processing system. Science. 330:845–851.

Georgopoulos A, Schwartz A, Kettner R. 1986. Neuronal population coding of movement direction. Science. 233:1416–1419.

Gobbini MI, Koralek AC, Bryan RE, Montgomery KJ, Haxby JV. 2007. Two takes on the social brain: a comparison of theory of mind tasks. J Cogn Neurosci. 19:1803–1814.

Graf ABA, Kohn A, Jazayeri M, Movshon JA. 2011. Decoding the activity of neuronal populations in macaque primary visual cortex. Nat Neurosci. 14:239–245.

Grill-Spector K, Weiner KS. 2014. The functional architecture of the ventral temporal cortex and its role in categorization. Nat Rev Neurosci. 15:536–548.

Grossman ED, Blake R. 2002. Brain areas active during visual perception of biological motion. Neuron. 35:1167–1175.

Guntupalli JS, Hanke M, Halchenko YO, Connolly AC, Ramadge PJ, Haxby JV. 2016. A model of representational spaces in human cortex. Cereb Cortex. 26:2919–2934.

Hanke M, Halchenko YO, Sederberg PB, Hanson SJ, Haxby JV, Pollmann S. 2009. PyMVPA: A python toolbox for multivariate pattern analysis of fMRI data. Neuroinformatics. 7:37–53.

Harel A, Kravitz DJ, Baker CI. 2014. Task context impacts visual object processing differentially across the cortex. Proc Natl Acad Sci USA. 111:E962–E971.

Hasson U, Nir Y, Levy I, Fuhrmann G, Malach R. 2004. Intersubject synchronization of cortical activity during natural vision. Science. 303:1634–1640.

Haxby JV, Connolly AC, Guntupalli JS. 2014. Decoding neural representational spaces using multivariate pattern analysis. Annu Rev Neurosci. 37:435–456.

Haxby JV, Gobbini MI, Furey ML, Ishai A, Schouten JL, Pietrini P. 2001. Distributed and overlapping representations of faces and objects in ventral temporal cortex. Science.

293:2425–2430.

Haxby JV, Guntupalli JS, Connolly AC, Halchenko YO, Conroy BR, Gobbini MI, Hanke M, Ramadge PJ. 2011. A common, high-dimensional model of the representational space in human ventral temporal cortex. Neuron. 72:404–416.

Henriksson L, Khaligh-Razavi S-M, Kay K, Kriegeskorte N. 2015. Visual representations are dominated by intrinsic fluctuations correlated between areas. NeuroImage. 114:275–286.

Hung CP, Kreiman G, Poggio T, DiCarlo JJ. 2005. Fast readout of object identity from macaque inferior temporal cortex. Science. 310:863–866.

Huth AG, de Heer WA, Griffiths TL, Theunissen FE, Gallant JL. 2016. Natural speech reveals the semantic maps that tile human cerebral cortex. Nature. 532:453–458.

Huth AG, Nishimoto S, Vu AT, Gallant JL. 2012. A continuous semantic space describes the representation of thousands of object and action categories across the human brain. Neuron. 76:1210–1224.

Jehee JFM, Brady DK, Tong F. 2011. Attention improves encoding of task-relevant features in the human visual cortex. J Neurosci. 31:8210–8219.

Kiani R, Esteky H, Mirpour K, Tanaka K. 2007. Object Category Structure in Response Patterns of Neuronal Population in Monkey Inferior Temporal Cortex. J Neurophysiol. 97:4296–4309.

Kriegeskorte N, Goebel R, Bandettini P. 2006. Information-based functional brain mapping. Proc Natl Acad Sci USA. 103:3863–3868.

Kriegeskorte N, Kievit RA. 2013. Representational geometry: integrating cognition, computation, and the brain. Trends Cogn Sci. 17:401–412.

Kriegeskorte N, Mur M, Bandettini P. 2008b. Representational similarity analysis—connecting the branches of systems neuroscience. Front Syst Neurosci. 2:4.

Kriegeskorte N, Mur M, Ruff DA, Kiani R, Bodurka J, Esteky H, Tanaka K, Bandettini PA. 2008a. Matching categorical object representations in inferior temporal cortex of man and monkey. Neuron. 60:1126–1141.

Kriegeskorte N, Simmons WK, Bellgowan PSF, Baker CI. 2009. Circular analysis in systems neuroscience: the dangers of double dipping. Nat Neurosci. 12:535–540.

Kruschke JK. 1992. ALCOVE: an exemplar-based connectionist model of category learning. Psychol Rev. 99:22–44.

Lange T, Roth V, Braun ML, Buhmann JM. 2004. Stability-based validation of clustering solutions. Neural Comput. 16:1299–1323.

Lewis JE, Kristan WB Jr. 1998. A neuronal network for computing population vectors in the leech. Nature. 391:76–79.

Marr D. 1982. Vision: A Computational Investigation Into the Human Representation and Processing of Visual Information. MIT Press.

Mitchell TM, Shinkareva SV, Carlson A, Chang K-M, Malave VL, Mason RA, Just MA. 2008. Predicting human brain activity associated with the meanings of nouns. Science. 320:1191–1195.

Miyawaki Y, Uchida H, Yamashita O, Sato M-A, Morito Y, Tanabe HC, Sadato N, Kamitani Y. 2008. Visual image reconstruction from human brain activity using a combination of multiscale local image decoders. Neuron. 60:915–929.

Nastase SA, Davis B, Halchenko YO, Hasson U. 2016. Cross-modal searchlight classification: methodological challenges and recommended solutions. In: 2016 International Workshop on Pattern Recognition in Neuroimaging (PRNI).

Nishimoto S, Shinji N, Vu AT, Thomas N, Yuval B, Bin Y, Gallant JL. 2011. Reconstructing visual experiences from brain activity evoked by natural movies. Curr Biol.

21:1641–1646.

Nosofsky RM. 1986. Attention, similarity, and the identification-categorization relationship. J Exp Psychol Gen. 115:39–57.

Oosterhof NN, Connolly AC, Haxby JV. 2016. CoSMoMVPA: multi-modal multivariate pattern analysis of neuroimaging data in Matlab/GNU Octave. Front Neuroinform. 10:27.

Oosterhof NN, Tipper SP, Downing PE. 2012. Viewpoint (in)dependence of action representations: an MVPA study. J Cogn Neurosci. 24:975–989.

Oosterhof NN, Tipper SP, Downing PE. 2013. Crossmodal and action-specific: neuroimaging the human mirror neuron system. Trends Cogn Sci. 17:311–318.

Oosterhof NN, Wiestler T, Downing PE, Diedrichsen J. 2011. A comparison of volume-based and surface-based multi-voxel pattern analysis. NeuroImage. 56:593–600.

Oosterhof NN, Wiggett AJ, Diedrichsen J, Tipper SP, Downing PE. 2010. Surface-based information mapping reveals crossmodal vision-action representations in human parietal and occipitotemporal cortex. J Neurophysiol. 104:1077–1089.

Pedregosa F, Varoquaux G, Gramfort A, Michel V, Thirion B, Grisel O, Blondel M, Prettenhofer P, Weiss R, Dubourg V, Vanderplas J, Passos A, Cournapeau D, Brucher M, Perrot M, Duchesnay E. 2011. Scikit-learn: Machine learning in Python. J Mach Learn Res. 12:2825–2830.

Peirce JW. 2007. PsychoPy—Psychophysics software in Python. J Neurosci Methods. 162:8–13.

Petersen SE, Posner MI. 2012. The attention system of the human brain: 20 years after. Annu Rev Neurosci. 35:73–89.

Reynolds JH, Heeger DJ. 2009. The normalization model of attention. Neuron. 61:168–185.

Reynolds JH, Pasternak T, Desimone R. 2000. Attention increases sensitivity of V4 neurons.

Neuron. 26:703–714.

Rigotti M, Barak O, Warden MR, Wang X-J, Daw ND, Miller EK, Fusi S. 2013. The importance of mixed selectivity in complex cognitive tasks. Nature. 497:585–590.

Rolls ET, Tovee MJ. 1995. Sparseness of the neuronal representation of stimuli in the primate temporal visual cortex. J Neurophysiol. 73:713–726.

Ruff DA, Cohen MR. 2014. Attention can either increase or decrease spike count correlations in visual cortex. Nat Neurosci. 17:1591–1597.

Russ BE, Leopold DA. 2015. Functional MRI mapping of dynamic visual features during natural viewing in the macaque. NeuroImage. 109:84–94.

Saad ZS, Reynolds RC, Argall B, Japee S, Cox RW. 2004. SUMA: An interface for surface-based intra- and inter-subject analysis with AFNI. In: 2004 IEEE International Symposium on Biomedical Imaging: From Macro to Nano.

Saltelli A, Tarantola S, Campolongo F, Ratto M. 2004. Sensitivity Analysis in Practice: A Guide to Assessing Scientific Models. John Wiley & Sons.

Serences JT, Boynton GM. 2007a. Feature-based attentional modulations in the absence of direct visual stimulation. Neuron. 55:301–312.

Serences JT, Boynton GM. 2007b. Feature-based attentional modulations in the absence of direct visual stimulation. Neuron. 55:301–312.

Sha L, Haxby JV, Abdi H, Guntupalli JS, Oosterhof NN, Halchenko YO, Connolly AC. 2015. The animacy continuum in the human ventral vision pathway. J Cogn Neurosci. 27:665–678.

Smith SM, Nichols TE. 2009. Threshold-free cluster enhancement: addressing problems of smoothing, threshold dependence and localisation in cluster inference. NeuroImage. 44:83–98.

Sprague TC, Serences JT. 2013. Attention modulates spatial priority maps in the human occipital, parietal and frontal cortices. Nat Neurosci. 16:1879–1887.

Thirion B, Varoquaux G, Dohmatob E, Poline J-B. 2014. Which fMRI clustering gives good brain parcellations? Front Neurosci. 8:167.

Treue S, Martínez Trujillo JC. 1999. Feature-based attention influences motion processing gain in macaque visual cortex. Nature. 399:575–579.

Tsotsos JK. 2011. A Computational Perspective on Visual Attention. Cambridge, MA: MIT Press.

Uchida N, Takahashi YK, Tanifuji M, Mori K. 2000. Odor maps in the mammalian olfactory bulb: domain organization and odorant structural features. Nat Neurosci. 3:1035–1043.

van den Berg R, Awh E, Ma WJ. 2014. Factorial comparison of working memory models. Psychol Rev. 121:124–149.

Yeo BTT, Krienen FM, Sepulcre J, Sabuncu MR, Lashkari D, Hollinshead M, Roffman JL, Smoller JW, Zollei L, Polimeni JR, Fischl B, Liu H, Buckner RL. 2011. The organization of the human cerebral cortex estimated by intrinsic functional connectivity. J Neurophysiol. 106:1125–1165.

Supplementary Material

Attention selectively reshapes the geometry of distributed semantic representation

Samuel A. Nastase, Andrew C. Connolly, Nikolaas N. Oosterhof, Yaroslav O. Halchenko, J. Swaroop Guntupalli, Matteo Visconti di Oleggio Castello, Jason Gors, M. Ida Gobbini, James V. Haxby

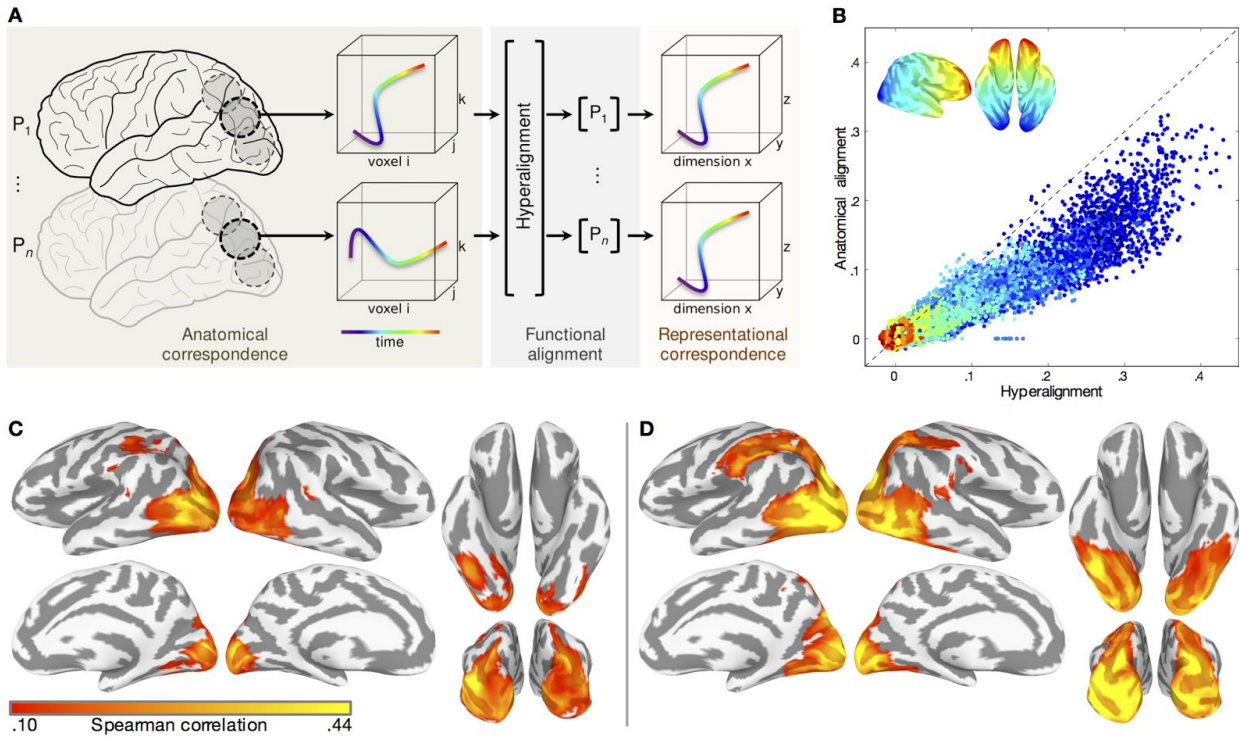

Supplementary Figure 1. Whole-brain searchlight hyperalignment enhances representational correspondence across participants. (*A*) For each surface-based searchlight, the Procrustes transformation is used to rotate each participant's time series of functional response patterns to the *Life* movie stimulus into a common space that maximizes representational correspondence across participants. These patterns are depicted as a trajectory of responses in a three-voxel space over time. (*B*) Each point in the scatterplot represents the average inter-participant Spearman correlation of RDMs for both attention tasks in a single searchlight. For each surface-based searchlight, the upper triangulars of the observed neural RDMs for both attention tasks were concatenated and pairwise Spearman correlations were computed between all participants. The vertical axis indicates Spearman correlation based on surface-based spherical alignment; the horizontal axis indicates Spearman correlation after surface-based searchlight whole-brain hyperalignment. Deviance

from the identity line indicates a strong effect of alignment method on inter-participant similarity of RDMs. Searchlights are colored according their location on the posterior–anterior axis of the inflated cortical surface. (*C*) Inter-participant Spearman correlation of searchlight RDMs for both attention tasks using anatomical alignment thresholded at .10. (*D*) Average inter-participant Spearman correlation of searchlight RDMs after hyperalignment at the same threshold. Prior to hyperalignment, the maximum mean Spearman correlation was .32 in a searchlight superior to the left lateral occipital sulcus. Following hyperalignment, the maximum mean Spearman correlation was .44 in a searchlight in the left lateral occipital sulcus.

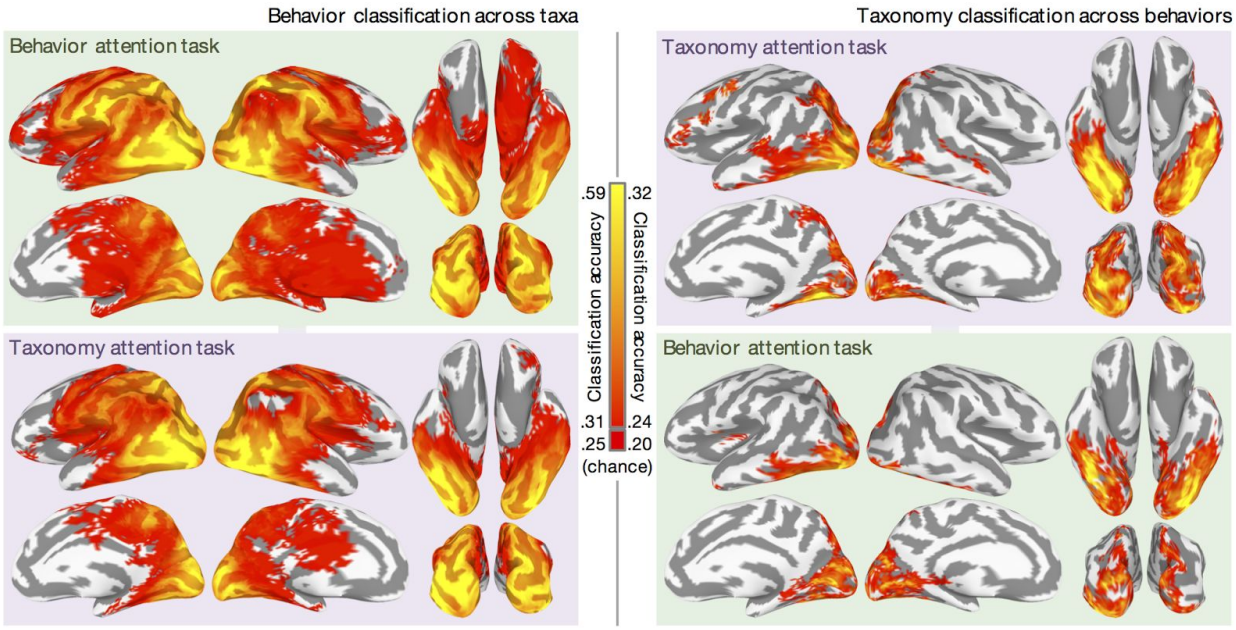

Supplementary Figure 2. Effect of attention on searchlight classification of behavior and taxonomy. Cross-validation was implemented in the following leave-one-category-out fashion: classifiers discriminating the four behaviors (left) were trained on four of the five taxa, and tested on the left-out taxon; classifiers discriminating the five animal taxa (right) were trained on three of the four behaviors and tested on the left-out behavior. This procedure ensured that any information about animal behavior generalizes across animal taxa, and vice versa. Furthermore, classifiers in this cross-validation scheme are always tested on exemplar clips not in the training set, ensuring that classification accuracy is not based solely on low-level visual properties idiosyncratic to particular stimuli. Prior to classification, the GLM was computed separately for each run, yielding 20 beta parameters per run. The maps are qualitatively similar to the representational similarity regression maps reported in Fig. 2, with an average correlation of .83 across conditions prior to thresholding. Chance accuracy for four-class behavior classification is .25 and chance accuracy for five-class taxonomy classification is .20. Accuracies less than 0.31 for behavior classification

and less than .24 for taxonomy classification are plotted as red. Maps are thresholded at $p < .05$ using TFCE, based on a null distribution of searchlight maps generated by permuting the labels of interest within each run and within each category of the crossed factor.

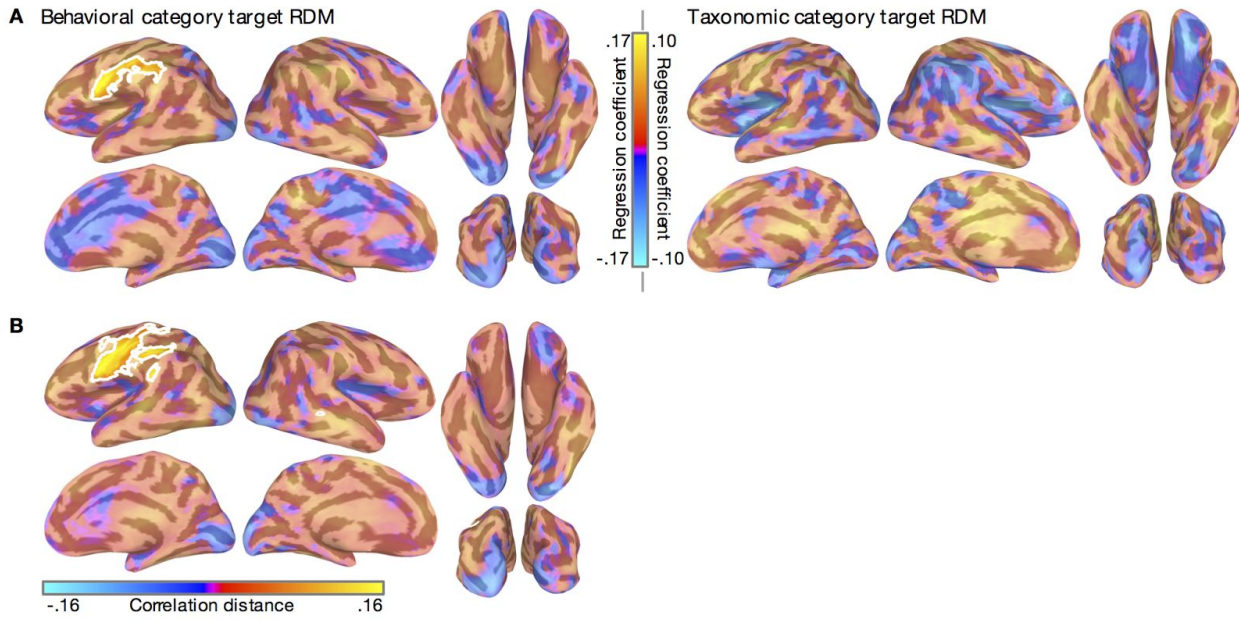

Supplementary Figure 3. Task differences in searchlight representational geometry. (*A*) Attention-related differences in standardized rank regression coefficients were computed for both the behavioral category and taxonomic category target RDMs. Warm colors represent attentional enhancement for the corresponding semantic information. The range of values on the color bar reflects the mean difference in the regression coefficient. (*B*) Cells of the searchlight RDMs capturing within-category distances for both animal behavior and taxonomy were isolated (see Fig. 4) and tested for attentional enhancement of correlation distance. The absolute values of the within-behavior and within-taxon distances were averaged for each searchlight to compute an index of overall task difference in within-category correlation distances. Clusters surviving TFCE-based correction for multiple comparisons at p = .05 (two-tailed test) are displayed at full opacity and outlined with a white contour, while searchlights not surviving TFCE are displayed as partially transparent. TFCE maps were estimated using a Monte Carlo simulation randomly flipping the attention task label. Note that the trend towards an effect of attention to taxonomy in VT cortex on

correlation with the taxonomic RDM was not significant in this searchlight analysis but was strongly significant in the ROI analysis that used larger regions. Searchlights in this case included only 100 voxels and cannot capture the more distributed effects observed in the ROI analysis. Furthermore, searchlight analyses are subjected to conservative multiple comparisons correction because of the large number of searchlights.

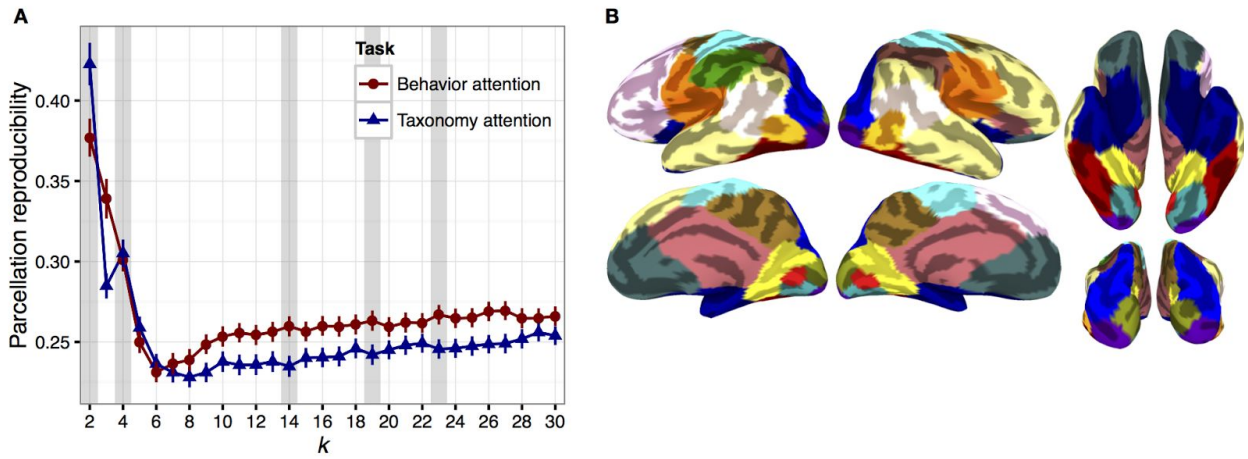

Supplementary Figure 4. Functional parcellation of the cerebral cortex based on representational geometry. (*A*) Parcellation reproducibility was evaluated using split-half resampling across participants (100 partitions per *k*) separately for each attention task. The mean AMI across the 100 partitions is plotted across the values of *k*, with error bars indicating the standard error of the mean across partitions. Vertical gray bars indicate several local maxima spanning the range of *k* tested. Parcellations at these reproducible values of *k* are visualized on the cortical surface in Supplementary Fig. 5. (*B*) Full parcellation at $k = 19$ for the behavior attention task data. Ten parcels from this solution corresponding to the dorsal and ventral visual pathways were further interrogated in the ROI analysis.

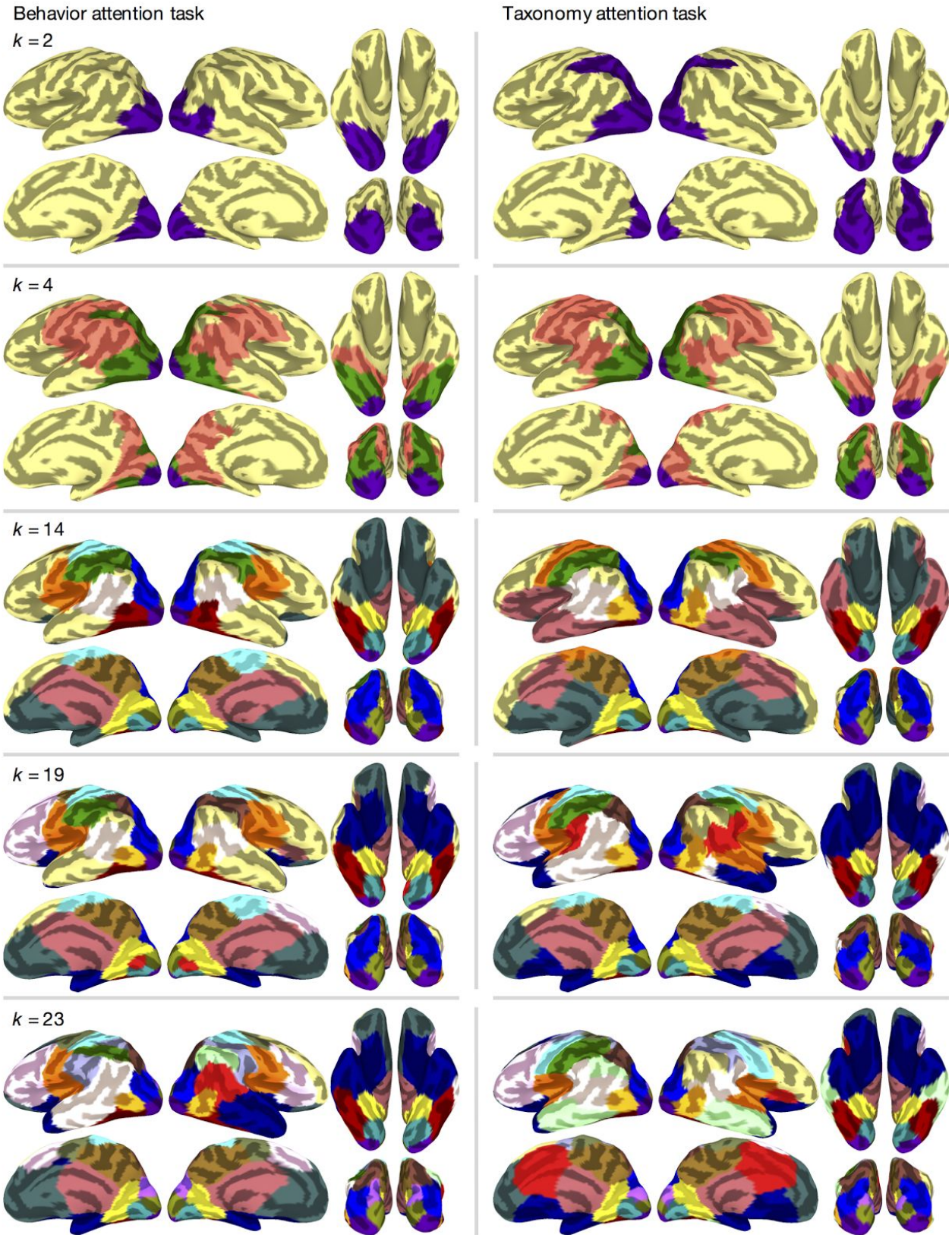
Behavior attention task
Taxonomy attention task
k = 2
k = 4
k = 14
k = 19
k = 23

Supplementary Figure 5. Functional parcellations at reproducible values of *k* for both attention tasks. Parcellation reproducibility was assessed using split-half resampling across participants, and parcellations are depicted for local maxima in parcellation reproducibility (*k* = 2, 4, 14, 19, and 23; corresponding to vertical gray bars in Supplementary Fig. 4*A*). The left column depicts parcellations based on searchlight representational geometries from the behavior attention task and the right column depicts parcellations based on searchlight representational geometries from the taxonomy attention task. The parcellation for the behavior attention task data (left) at *k* = 19 was used for subsequent ROI analysis and is reproduced in Fig. 3 and Supplementary Fig. 4*B*. Colors were assigned manually to avoid similar colors at anatomically adjacent parcels, and to emphasize similar parcels across tasks and values of *k*.

Description	Behavioral category	Taxonomic category
Chimpanzee eating a fruit	Eating	Primate
Howler monkey eating leaves	Eating	Primate
Llama eating cactus fruits	Eating	Ungulate
Reindeer grazing on grass	Eating	Ungulate
Lammergeier eating carrion	Eating	Bird
Hummingbird drinking from flower	Eating	Bird
Chameleon eating grasshopper	Eating	Reptile
Komodo dragon eating carcass	Eating	Reptile
Caterpillar eating its own eggshell	Eating	Insect
Ladybug eating mites	Eating	Insect
Baboons fighting on rocks	Fighting	Primate
Geladas fighting amongst herd	Fighting	Primate
Bison butting heads on prairie	Fighting	Ungulate
Ibex locking horns on mountainside	Fighting	Ungulate
Seabirds fighting on rocks	Fighting	Bird
Vultures fighting in the snow	Fighting	Bird
Chameleon biting another chameleon	Fighting	Reptile
Komodo dragons fighting	Fighting	Reptile
Ant and ladybug fighting	Fighting	Insect
Stag beetles locking mandibles	Fighting	Insect
Baboon running toward water	Running	Primate
Monkey running away through tall grass	Running	Primate
Juvenile ibex running down mountainside	Running	Ungulate
Topi running through herd	Running	Ungulate
Penguin running across meadow	Running	Bird
Seagull running through cloud of insects	Running	Bird
Komodo dragon walking on rocks	Running	Reptile
Lizard running across sand	Running	Reptile
Ants traveling across sand	Running	Insect
Beatle running across dirt	Running	Insect
Macaque swimming underwater	Swimming	Primate
Snow monkey swimming in hot spring	Swimming	Primate
Deer swimming across lake	Swimming	Ungulate
Reindeer herd swimming across strait	Swimming	Ungulate
Duck swimming across stream	Swimming	Bird
Penguin swimming underwater	Swimming	Bird
Marine iguana swimming in clear water	Swimming	Reptile

Sea turtle swimming near seafloor	Swimming	Reptile
Dobsonfly larva swimming toward streambed	Swimming	Insect
Water beetle swimming underwater	Swimming	Insect

Supplementary Table 1. Descriptions of video clip stimuli and condition assignments. Each of the 40 video clip exemplars is briefly described. The condition assignments are indicated for each clip. There were two exemplar clips for each condition.

Parcel	Color	Extent	Task differences in Spearman's ρ (z-value)	
			Behavior RDM	Taxonomy RDM
pEV	purple	1,419	-0.944	0.914
iEV	teal	1,321	-0.928	-0.191
sEV	olive	1,220	-2.142*	-0.798
aEV	red	882	-0.863	0.922
LO	gold	1,333	1.652	1.707
VT	maroon	2,063	2.326*	2.567*
OP	blue	3,570	0.372	0.223
IPS	copper	2,638	2.535*	0.770
Left PCS	green	1,356	2.784**	2.095*
vPC/PM	orange	3,995	2.228*	0.649
dPC	cyan	4,840	2.385*	2.221*
pSTS	white	2,793	1.135	0.365
Right dlPFC	light yellow	11,362	1.579	0.846
Left dlPFC	violet	5,199	1.856	0.739
mV	yellow	2,671	-0.211	0.434
Precuneus	brown	4,428	1.933	1.238
Cingulate	dark pink	3,166	1.731	0.909
OFC	navy	5,611	1.656	0.849
mPFC	dark gray	3,334	0.190	0.425

Supplementary Table 2. Task differences in Spearman correlation for all 19 parcels (Fig. 3). Parcels are listed roughly proceeding from posterior early visual areas anteriorly along the lateral surface, followed by medial structures. Parcel colors reference Supplementary Fig. 4*B*. Extent indicates the number of voxels referenced by all surface-based searchlights in the parcel. The average extent across all 19 parcels was 3,260 voxels (SD = 2,378 voxels). Note that neighboring searchlights overlap spatially and may overlap in the voxels they reference, although these voxels are only counted once for analysis purposes and in each parcel's extent. Task differences in representational geometry were evaluated by applying (exact) permutation tests to the Fisher transformed Spearman correlations between the observed neural RDM for each parcel and the behavioral category and taxonomic category target

RDMs. Reported z-values were derived from the *p*-values returned by the nonparametric randomization test. Negative values indicate decreased Spearman correlation with a target RDM when attending to the corresponding semantic information. Parcel label abbreviations are as follows. pEV: bilateral posterior early visual cortex comprising the occipital pole and posterior lateral occipital sulcus; iEV: bilateral inferior early visual cortex extending from the inferior bank of the posterior calcarine sulcus across the posterior lingual gyrus and posterior transverse collateral sulcus to the inferior occipital gyrus; sEV: bilateral superior early visual cortex encompassing the posterior calcarine sulcus and posterior cuneus; aEV: bilateral anterior early visual cortex including the anterior calcarine sulcus and a portion of the lingual gyrus; LO: bilateral lateral occipitotemporal cortex including the inferior middle occipital gyrus (and human MT+); VT: bilateral ventral temporal cortex including the fusiform gyrus, inferior temporal gyrus, and lateral occipitotemporal sulcus; OP: bilateral occipitoparietal and posterior parietal cortex extending from the lateral occipital sulcus dorsally to the transverse parietal sulcus; IPS: bilateral anterior intraparietal sulcus including the superior parietal lobule; left PCS: left postcentral sulcus, including the postcentral gyrus, inferior parietal lobule (supramarginal gyrus), and anterior intraparietal sulcus; vPC/PM: bilateral ventral pericentral gyri including the ventral central sulcus, premotor cortex, and extending ventrally to include the subcentral gyrus and posterior insula; dPC: bilateral dorsal pericentral gyri and central sulcus extending medially to the paracentral gyrus and posterior medial frontal gyrus; pSTS: bilateral posterior superior temporal sulcus including the posterior middle temporal gyrus and superior temporal gyrus; left dlPFC: left dorsolateral prefrontal cortex extending from the superior frontal gyrus ventrally to the inferior frontal gyrus and extending dorsomedially to the middle anterior medial superior frontal cortex; right dlPFC: right dorsolateral prefrontal cortex extending from the superior frontal gyrus ventrally to inferior

frontal gyrus and extending dorsomedially to middle-anterior medial superior frontal cortex, as well as bilateral anterior superior temporal sulcus (aSTS) and middle temporal gyrus, and bilateral temporoparietal junction (TPJ), including the inferior parietal lobule, supramarginal gyrus, and angular gyrus; mV: bilateral medial visual cortex extending from the parietooccipital sulcus across the anterior calcarine sulcus to the parahippocampal gyrus and medial aspect of the fusiform gyrus; Precuneus: bilateral precuneus including subparietal cortex and the marginal ramus of the cingulate sulcus, as well as the bilateral posterior superior frontal sulcus; Cingulate: bilateral middle cingulate cortex, medial subcortical structures, and the right anterior insula; OFC: bilateral orbitofrontal cortex extending posteriorly to include bilateral anterior temporal lobes (ATL; parahippocampal gyrus and temporal pole); mPFC: bilateral medial prefrontal cortex including the anterior cingulate and superior frontal gyrus. See Supplementary Table 3 for tests computed separately for each bilateral homologue and otherwise anatomically discontiguous parcel. *$p < .05$, **$p < .01$, two-sided nonparametric randomization test, uncorrected.

Parcel	Hemisphere	Color	Extent	Task differences in Spearman's ρ (z-value)	
				Action RDM	Animal RDM
pEV	L	purple	712	-1.309	-0.098
	R	purple	707	-0.827	0.596
iEV	L	teal	729	-0.233	0.681
	R	teal	552	-1.414	-0.777
sEV	L	olive	654	-2.235*	-1.162
	R	olive	566	-1.725	-0.991
aEV	L	red	470	0.191	1.917
	R	red	412	-1.339	-1.285
LO	L	gold	592	2.034*	1.411
	R	gold	741	0.061	0.771
VT	L	maroon	1,037	2.308*	2.038*
	R	maroon	1,026	1.929	2.001*
OP	L	blue	1,878	0.474	0.406
	R	blue	1,692	0.328	0.408
IPS	L	copper	980	0.378	0.130
	R	copper	1,658	2.602**	0.692
Left PCS	L	green	1,356	2.784**	2.095*
vPC/PM	L	orange	1,953	2.354*	1.135
	R	orange	2,042	1.454	0.125
dPC	L	cyan	2,616	2.074*	2.160*
	R	cyan	2,224	1.704	2.095*
pSTS	L	white	1,300	1.921	0.283
	R	white	1,493	0.435	0.553
Right dlPFC	R	light yellow	5,004	1.532	0.562
aSTS	L	light yellow	1,726	1.048	0.853
	R	light yellow	2,169	1.461	0.906
TPJ	L	light yellow	766	1.630	0.845
	R	light yellow	1,117	1.488	-0.113
Left OFC	L	light yellow	195	0.162	-0.101
Right aI	R	light yellow	138	1.691	-0.070
Left PreC	L	light yellow	127	1.962*	2.166*
Left dlPFC	L	violet	5,199	1.856	0.739
mV	L	yellow	1,374	-0.261	0.511
	R	yellow	1,297	0.112	0.494

Precuneus	L	brown	1,440	0.831	0.742
	R	brown	1,449	1.126	0.851
pSFS	L	brown	803	3.487***	1.546
	R	brown	653	0.465	0.062
Cingulate	L	pink	1,380	0.677	1.358
	R	pink	1,234	1.725	0.841
Left aI	L	pink	552	2.079*	-0.569
OFC	L	navy	2,275	1.393	0.905
	R	navy	2,083	1.550	0.578
mPFC	L	dark gray	1,649	0.507	0.579
	R	dark gray	1,685	0.077	0.287

Supplementary Table 3. Task differences in Spearman correlation computed separately for each anatomically discontiguous parcel. In many cases, the clustering algorithm returned bilateral homologues as one cluster, while in several cases additional spatially discontiguous regions of the cortical surface were included in a single cluster. We split these discontiguous regions into separate parcels based on the neighborhood structure of the cortical surface mesh, then analyzed each parcel separately using nonparametric randomization tests. The average extent across all discontiguous parcels was 1,394 voxels (SD = 1,026 voxels). Z-values were derived from the *p*-values returned by the randomization test, and negative values indicate decreased Spearman correlation with a target RDM when attending to the corresponding semantic categories. In addition to bilateral homologues, the highly diffuse right dlPFC cluster split into bilateral anterior superior temporal sulcus (aSTS) parcels, bilateral temporoparietal junction (TPJ) parcels, and three small parcels in left orbitofrontal cortex (OFC), right anterior insula (aI), and left precentral gyrus (PreC). The Precuneus cluster included bilateral posterior superior frontal sulcus (pSFS) parcels, and the Cingulate cluster included a portion of the left anterior insula (aI). *$p < .05$, **$p < .01$, ***$p < .005$, two-sided nonparametric randomization test, uncorrected.

Parcel	Task enhancement for within-category distances	
	Within-behavior	Within-taxon
pEV	-1.287	0.606
iEV	-0.664	0.145
sEV	-2.200*	-0.659
aEV	-0.696	0.534
LO	0.899	1.586
VT	2.200*	2.620**
OP	0.563	1.301
IPS	1.917	1.390
Left PCS	3.097***	2.584**
vPC/PM	2.705**	1.134
dPC	2.090*	2.620**
pSTS	0.632	0.382
Right dlPFC	1.770	1.113
Left dlPFC	1.617	1.023
mV	-0.452	0.669
Precuneus	1.873	1.542
Cingulate	1.501	1.278
OFC	1.669	1.207
mPFC	0.579	0.781

Supplementary Table 4. Task enhancement for within-category correlation distances for all 19 parcels (Fig. 4). Reported z-values were derived from the *p*-values returned by the nonparametric randomization test. Positive values in the "within-behavior" column can be interpreted as either decreased within-behavioral category distances when attending to behavior or an increase in between-taxonomic category distances when attending to taxonomy; similarly, positive values in the "within-taxonomy" column can be interpreted as either decreased within-taxonomic category distances when attending to taxonomy or increased between-behavioral category distances when attending to behavior. Negative values indicate the inverse effect. See Supplementary Table 5 for tests computed separately

for each bilateral homologue and otherwise anatomically discontiguous parcel. $^{*}p < .05$, $^{**}p < .01$, $^{***}p < .005$, two-sided nonparametric randomization test, uncorrected.

Parcel	Hemisphere	Task enhancement for within-category distances	
		Within-behavior	Within-taxon
pEV	L	-1.601	-0.391
	R	-1.036	0.323
iEV	L	-0.094	0.376
	R	-0.794	-0.278
sEV	L	-2.221*	-0.985
	R	-2.019	-0.669
aEV	L	0.141	1.385
	R	-1.001	-0.994
LO	L	1.918	1.461
	R	-0.582	0.866
VT	L	2.364*	2.221*
	R	1.084	2.124*
OP	L	1.301	1.230
	R	-0.341	0.948
IPS	L	0.937	1.270
	R	1.891	0.241
Left PCS	L	3.097***	2.584**
vPC/PM	L	2.848**	1.626
	R	2.186*	0.377
dPC	L	1.941	2.640**
	R	1.600	2.015*
pSTS	L	1.499	0.470
	R	-0.024	0.407
Right dlPFC	R	1.623	0.908
aSTS	L	1.048	0.853
	R	1.461	0.906
TPJ	L	1.059	1.005
	R	1.396	1.431
Left OFC	L	0.292	-0.115
Right aI	R	1.856	-0.029
Left PreC	L	2.048*	2.243*
Left dlPFC	L	1.617	1.023
mV	L	-0.050	0.674
	R	0.254	0.314

Precuneus	L	0.836	0.855
	R	1.319	1.122
pSFS	L	3.182***	1.280
	R	0.997	0.446
Cingulate	L	0.602	1.430
	R	1.538	1.144
Left aI	L	1.895	-0.036
OFC	L	1.450	1.218
	R	1.546	1.033
mPFC	L	0.642	0.781
	R	0.493	0.728

Supplementary Table 5. Task enhancement for within-category distances computed separately for each anatomically discontiguous parcel. In addition to bilateral homologues, the highly diffuse right dlPFC cluster split into bilateral anterior superior temporal sulcus (aSTS) parcels, bilateral temporoparietal junction (TPJ) parcels, and three small parcels in left orbitofrontal cortex (OFC), right anterior insula (aI), and left precentral gyrus (PreC). The Precuneus cluster included bilateral posterior superior frontal sulcus (pSFS) parcels, and the Cingulate cluster included a portion of the left anterior insula (aI). *$p < .05$, **$p < .01$, ***$p < .005$, two-sided nonparametric randomization test, uncorrected.